BNL-107476-2015-JA

Cosmology Constraints from the Weak Lensing Peak Counts and the Power Spectrum in CFHTLenS

Jia Liu[1],* Andrea Petri[2],† Zoltán Haiman[1,3],‡ Lam Hui[2,3],§ Jan M. Kratochvil[4],¶ and Morgan May[5]**
[1] *Department of Astronomy and Astrophysics, Columbia University, New York, NY 10027, USA*
[2] *Department of Physics, Columbia University, New York, NY 10027, USA*
[3] *Institute for Strings, Cosmology, and Astroparticle Physics (ISCAP), Columbia University, New York, NY 10027, USA*
[4] *Astrophysics and Cosmology Research Unit, University of KwaZulu-Natal, Westville, Durban, 4000, South Africa and*
[5] *Physics Department, Brookhaven National Laboratory, Upton, NY 11973, USA*
(Dated: January 19, 2015)

Lensing peaks have been proposed as a useful statistic, containing cosmological information from non-Gaussianities that is inaccessible from traditional two-point statistics such as the power spectrum or two-point correlation functions. Here we examine constraints on cosmological parameters from weak lensing peak counts, using the publicly available data from the 154 deg^2 CFHTLenS survey. We utilize a new suite of ray-tracing N-body simulations on a grid of 91 cosmological models, covering broad ranges of the three parameters Ω_m, σ_8, and w, and replicating the galaxy sky positions, redshifts, and shape noise in the CFHTLenS observations. We then build an emulator that interpolates the power spectrum and the peak counts to an accuracy of $\leq 5\%$, and compute the likelihood in the three-dimensional parameter space (Ω_m, σ_8, w) from both observables. We find that constraints from peak counts are comparable to those from the power spectrum, and somewhat tighter when different smoothing scales are combined. Neither observable can constrain w without external data. When the power spectrum and peak counts are combined, the area of the error "banana" in the (Ω_m, σ_8) plane reduces by a factor of $\approx$ two, compared to using the power spectrum alone. For a flat Λ cold dark matter model, combining both statistics, we obtain the constraint $\sigma_8(\Omega_m/0.27)^{0.63} = 0.85^{+0.03}_{-0.03}$.

PACS numbers: PACS codes: 98.80.-k, 95.36.+x, 95.30.Sf, 98.62.Sb

I. INTRODUCTION

Weak gravitational lensing (WL) is one of the most promising techniques to probe dark energy (DE) with improved precision in the future (see recent reviews by [1–5]). By statistically measuring the distortions in the shapes of background galaxies, the matter density fluctuations at different redshifts can be mapped, yielding constraints on the parameters of the background cosmological model. Pioneering WL surveys, such as the Cosmic Evolution Survey (COSMOS, [6]) and the Canada-France-Hawaii Telescope Lensing Survey (CFHTLenS, [7, 8]) have recently successfully demonstrated the utility of this technique, yielding constraints on the matter density Ω_m and fluctuation amplitude σ_8 comparable with other existing methods, even with relatively small sky coverage (~ 1 and 154 deg^2, respectively).

In this paper, we use the publicly available CFHTLenS data on ≈ 4.2 million galaxies, combined with a suite of ray-tracing simulations in 91 different cosmological models, to constrain the cosmological parameters, Ω_m, σ_8, and the DE equation of state w. Traditionally, WL data is analyzed using the two-point correlation function (2PCF), or its Fourier-space counterpart, the power spectrum. However, these statistics can not fully characterize the weak lensing shear field on small ($\lesssim$ arcmin) angular scales, where it is sensitive to matter density fluctuations in the non-linear regime, and is strongly non-Gaussian. Various non-Gaussian statistics (e.g. higher moments [9, 11, 15, 16, 18, 21], three-point functions [17, 26], bispectra [19, 20, 22, 24], peak counts [14, 23, 25, 27, 28], or Minkowski functionals [29, 55]) have been proposed in the past, and shown to improve cosmological constraints from WL surveys.

In this work, we focus on peak statistics, which describe the distribution of local maxima in a convergence map, as a function of peak height. It is a particularly simple statistic, forecasted to yield a factor of $\sim$ two improvement on cosmological parameters when combined with two-point statistics by several recent studies [30–34], and also found to be unusually robust to systematic errors from baryonic effects [34]. In a companion paper (Petri et al. in prep) we examine constraints from Minkowski functionals and higher moments of the WL convergence field.

A handful of works have recently begun to examine non-Gaussian features in the CFHTLenS data. Three-point statistics have been measured in both CFHTLenS [35] and earlier in COSMOS [36] and found to lead to modest (up to $\approx 10\%$) improvements on the combination $\sigma_8\Omega_m^\alpha$ with $\alpha \approx 0.3 - 0.5$. Ref. [37] measured Minkowski functionals in CFHTLenS and showed that

* jia@astro.columbia.edu
† apetri@phys.columbia.edu
‡ zoltan@astro.columbia.edu
§ lhui@astro.columbia.edu
¶ kratochvilj@ukzn.ac.za
** may@bnl.gov

they can break degeneracies among cosmological parameters, improving constraints on Ω_m and σ_8. Finally, higher moments [38] and peak counts [39] have both been measured in CFHTLenS , although cosmological constraints have not yet been derived from them.

The distinguishing feature of the present work is that we compute peak count statistics, including their dependence on cosmology and their variance, from simulations in a large number of cosmological models (91 in total). Simulating multiple cosmological models is necessary because analytical predictions of peak counts for non-Gaussian fields are still in early development (for example, Ref.[40]). simulating multiple cosmological models is necessary. Furthermore, a large number ($\gtrsim$ hundreds) of realizations per model is necessary to measure the covariance of the peak counts, and to compute accurate confidence limits on cosmological parameters. Because of computational limitations, most works on non-Gaussian WL statistics to date have sampled only a few points in the multi-dimensional cosmological parameter space, and assumed a linear dependence on cosmological parameters to compute observables in other cosmologies (effectively implementing a numerical version of a Fisher matrix) or else relied on fitting formulae calibrated with a handful of simulations. The only exception we are aware of is Ref. [30], who studied peak counts in simulations on a two-dimensional Ω_m, σ_8 grid, and whose results already indicate that the Ω_m and σ_8 dependence is non-linear, and the Fisher approach is therefore highly inaccurate.

Recently, a series of papers dubbed "the Coyote Universe" [41–44] have built an emulator, based on a large number of simulations, to address analogous issues for the matter power spectrum. Using 37 cosmological models, these studies have shown that the matter power spectrum can be interpolated and computed to 1% accuracy out to $k \sim 1$ Mpc^{-1} for models in-between the simulated points in parameter space. We have built an emulator following a similar approach, but describing WL observables, and tailored specifically for the CFHTLenS fields. Unlike in a general–purpose emulator, galaxy properties (e.g. redshift distribution, position, and noise) are not freely adjustable parameters, but rather fixed and built into our simulations from the outset, adapted directly from the CFHTLenS measurements.

The paper is structured as follows. We first describe CFHTLenS data processing and convergence map construction in § II, and our ray-tracing simulations and numerical details in § III. We present the results of our analysis in § IV, and we offer our conclusions in § V.

II. CFHTLENS DATA PROCESSING

The 154 deg^2 CFHTLenS data cover four individual patches on the sky, with an area of 64, 23, 44 and 23 deg^2 for field W1, W2, W3 and W4, respectively. The CFHTLenS data analysis roughly consists of: (1) creation of the galaxy catalogue using SExtractor [45]; (2) the photometric redshift estimation with a Bayesian photometric redshift code [46] ; (3) galaxy shape measurement with *lens*fit [47, 48]; and finally (4) cosmological analysis with 2PCF [8]. A summary of the data analysis process is listed in Appendix C of Ref. [45]. We refer the readers to the CFHTLenS papers mentioned above for more technical details.

We apply the following cuts to galaxies: mask ≤ 1 (see Table B2 in Ref. [45] for the meaning of mask values), redshift $0.2 < z < 1.3$, fitclass $= 0$ (requiring the object to be a galaxy), and weight $\mathcal{W} > 0$ (with larger $\mathcal{W}$ indicating smaller shear measurement uncertainty). Applying these cuts leaves us 4.2 million galaxies, 124.7 deg^2 sky, and average number density $n_{gal} \approx 9.3$ arcmin^{-2}.

A. Map Projection and Smoothing

Because the CFHTLenS fields are irregularly shaped, and because we ray-trace to the actual observed galaxy positions, we first divide them into 13 squares (subfields) to match the square shape and ≈12 deg^2 size of our simulated maps. Fig. 1 shows the convergence maps for the CFHTLenS fields, as well as the divisions into subfields. To maximize the data usage, three subfields are each composed of two physically separated sky patches (the ones with rectangular shape in the figure).

Galaxies in each subfield are then placed on a 512×512 pixel grid using the flat sky (Gnomonic) projection [49],

$$x = \frac{\cos\phi \sin(\lambda - \lambda_0)}{\cos\eta}, \tag{1}$$

$$y = \frac{\cos\phi_0 \sin\phi - \sin\phi_0 \cos\phi \cos(\lambda - \lambda_0)}{\cos\eta} \tag{2}$$

where (x, y) is the galaxy position in radians on the grid map, (λ, ϕ) the position in (RA, Dec), (λ_0, ϕ_0) the center of the subfield, and η the angular distance from the center,

$$\cos\eta = \sin\phi_0 \sin\phi + \cos\phi_0 \cos\phi \cos(\lambda - \lambda_0). \tag{3}$$

In order to reduce the noise and to perform a Fourier transform, we use a Gaussian window function to smooth the grid map,

$$\overline{\boldsymbol{e}}(\boldsymbol{\theta_0}) = \frac{\int d^2\theta W(|\boldsymbol{\theta} - \boldsymbol{\theta_0}|)\mathcal{W}(\boldsymbol{\theta}) \left[\boldsymbol{e}^{\rm obs}(\boldsymbol{\theta}) - \boldsymbol{c}(\boldsymbol{\theta})\right]}{\int d^2\theta W(|\boldsymbol{\theta} - \boldsymbol{\theta_0}|)\mathcal{W}(\boldsymbol{\theta})[1 + m(\boldsymbol{\theta})]} \tag{4}$$

$$W(\theta) = \frac{1}{2\pi\theta_G^2} \exp(-\frac{\theta^2}{2\theta_G^2}), \tag{5}$$

where $\overline{\boldsymbol{e}}(\boldsymbol{\theta_0})$ is the smoothed complex ellipticity $\boldsymbol{e} = e_1 + ie_2$ at the pixel $\boldsymbol{\theta_0}$. $W(\theta)$ is the Gaussian smoothing window with scale θ_G, which we choose to be 0.5, 1.0, 1.8, 3.5, 5.3, and 8.9 arcmin. $\mathcal{W}$ is the *lens*fit weight for each galaxy. c and m are additive and multiplicative corrections, which we include following Refs. [47, 48],

$$\boldsymbol{e}^{\rm obs} = (1 + m)\boldsymbol{e}^{\rm true} + \boldsymbol{c}. \tag{6}$$

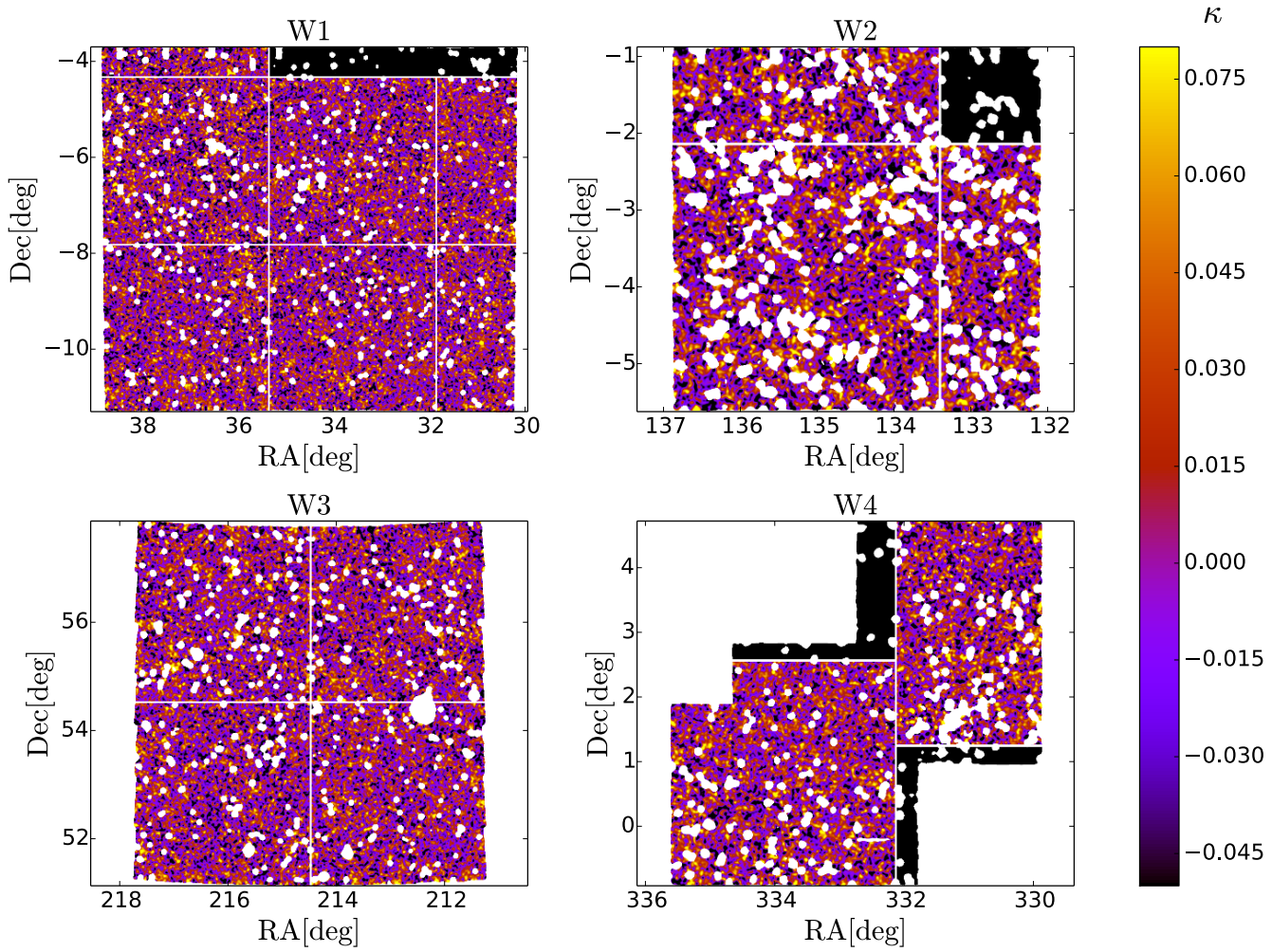

FIG. 1. Convergence maps for the four CFHTLenS fields. They are divided into 13 subfields of 12 deg^2 in size to match our simulation configuration. Scattered white dots are masks. White lines mark the edges of our simulated maps. Three subfields are collages of the six rectangular patches in W1, W2, W4. Patches in black and white are not used in our simulation.

The additive correction $\boldsymbol{c}$ is consistent with 0 for e_1, and < 0.05 for e_2, and m is a function of signal-to-noise ($\nu_{\rm SN}$) and galaxy size (r),

$$m(\nu_{\rm SN}, r) = \frac{\beta}{\log_{10}(\nu_{\rm SN})} \exp(-\alpha r \nu_{\rm SN}), \qquad (7)$$

with $\alpha = 0.057$ and $\beta = -0.37$. This multiplicative correction for each galaxy (denominator of eq. 4) is a fit to the ensemble average over galaxies within the window function, because the result can be unstable on a galaxy–by–galaxy basis when $(1+m) \to 0$. We tested the impact of the m calibration following § 8.5 of Ref. [48]. We sampled 100 sets of random (α, β) values from their probability distribution provided in Ref. [48], and computed the variance of the power spectrum and the peak counts among these 100 samples. Similar to the results of the analysis in Ref. [48] for the 2PCF, we found that this calibration impacts the power spectrum and the peak counts at the $\lesssim 10^{-3}$ level, negligible comparing to the variance between random realizations of the underlying lensing maps.

B. Convergence Map Construction and Masking

The convergence (κ) and the complex shear ($\boldsymbol{\gamma} = \gamma_1 + i\gamma_2$) are obtained from derivatives of the lensing potential

(ψ). They are defined as

$$\kappa(\boldsymbol{\theta}) = \frac{1}{2}\nabla^2\psi(\boldsymbol{\theta}), \quad (8)$$

$$\gamma_1(\boldsymbol{\theta}) = \frac{1}{2}(\psi_{,11} - \psi_{,22}), \quad (9)$$

$$\gamma_2(\boldsymbol{\theta}) = \psi_{,12}, \quad (10)$$

where indices separated by a comma denote partial derivatives with respect to two orthogonal components θ_1 and θ_2 of $\boldsymbol{\theta}$. We can reconstruct the convergence map from shear measurements [50] using,

$$\hat{\kappa}(\boldsymbol{\ell}) = \left(\frac{\ell_1^2 - \ell_2^2}{\ell_1^2 + \ell_2^2}\right)\hat{\gamma}_1(\boldsymbol{\ell}) + 2\left(\frac{\ell_1\ell_2}{\ell_1^2 + \ell_2^2}\right)\hat{\gamma}_2(\boldsymbol{\ell}) \quad (11)$$

where $\hat{\kappa}$, $\hat{\gamma}$ are the convergence and the shear in Fourier space, and $\boldsymbol{\ell}$ is the wave vector with components ℓ_1, ℓ_2. Note that ellipticity is used as a measure of the shear, using the weak lensing approximation ($\langle \boldsymbol{e} \rangle = \boldsymbol{\gamma}$; see below).

The data contain unusable regions (due to bright stars and bad pixels). These regions and sky patches with low galaxy number density can induce large errors and noise (e.g. [51–53]). Hence we mask them out (shown as the scattered white dots in Fig. 1). By masking out low density regions, we assume there is no correlation between the lensing signal and the galaxy number density, i.e. neglecting the magnification bias. Ref. [54] found that the magnification bias has negligible impact on cosmological parameters for surveys with < 1000 deg^2 coverage. To generate masks, we first create grid maps of the same size and resolution as the convergence maps, but with each pixel containing the number of galaxies (n_{gal}) falling within that pixel. We then smooth this galaxy surface density map with the same Gaussian window function as before (Eq. 5). Finally, we remove regions where $n_{gal} < 5$ arcmin^{-2} (see Ref. [37]). In order to perform a Fourier transform on the resulting maps, we set all pixels within the masked regions to zero. This can introduce noise at small scales, and we limit our final analysis to scales $\ell < 7,000$. We also apply the same procedure on the simulated maps.

C. Power Spectrum and Peak Counts

The power spectrum is the Fourier counterpart of the two-point correlation function. We first Fourier transform the convergence map (with 0.5 arcmin smoothing scale), and then average over all spherical harmonics ($\ell = |\boldsymbol{\ell}|$) to obtain the power spectrum, with 40 equally spaced log bins in the range $370 < \ell < 25,000$.

Peak counting is done by scanning through the pixels on the convergence map, and identifying local maxima (pixels with a higher value of κ than its surrounding 8 pixels). We then record the number of peaks as a function of their central κ value. In our analysis, we use peaks with $-0.04 < \kappa < 0.12$ and test various smoothing scales.

The final power spectrum is averaged over the 13 subfields, weighted by the number of galaxies in each subfield. The final peak counts is the sum over 13 subfields.

III. THE EMULATOR

The construction of the emulator consists of three steps. First, we sample 91 points using the latin hypercube method in the three-dimensional (3D) parameter space within the broad ranges $0 < \Omega_m < 1$, $-3 < w < 0$, and $0.1 < \sigma_8 < 1.5$. For each sampled point, we run an N-body simulation and perform ray-tracing to create shear maps that are directly comparable to the CFHTLenS data. Second, we create convergence maps, measure the power spectra and peak counts, and interpolate between the 91 simulated grid points to make predictions for arbitrary cosmological models within the simulated range. Finally, we compute the parameter likelihood in the 3D space (Ω_m, w, σ_8) to find the best fit values and marginalized confidence contours, using the CFHTLenS observations.

A. N-body simulation and ray-tracing

We first pick 91 sampling points that are spread out in the 3D space as evenly as possible, but not overlap when projected on 2D or 1D space. To do this, we use the latin hypercube sampling method following Ref. [42]. A list of parameters residing on a diagonal line is first generated, and then randomly shuffled on each dimension. For a random pair of points and a random parameter, we swap their values. The last step was repeated until we reached convergence in average distance between the points (10^5 iterations). The resulting parameter values are listed in Table I and shown visually in Figure 2.

We then run one N-body simulation at each sampling point, using a modified version of the Gadget-2 code[1]. Except for the values of the three cosmological parameters, the parameters and setup of these N-body simulations are the same as used in our earlier work [27, 29, 31, 34, 54–56]. We refer readers to these papers for more detailed information. The simulations have a box size of $240h^{-1}$ comoving Mpc, containing 512^3 dark matter particles. This corresponds to a mass resolution of $7.4 \times 10^9 h^{-1} M_\odot$. We set the Hubble constant $h = 0.72$, baryon density $\Omega_b h^2 = 0.0227$, and the spectral index $n_s = 0.96$. We compute the initial (linear) total matter power spectrum with the Einstein-Boltzmann code CAMB[2] [57] at $z = 0$ and scale it back to initial redshift $z = 100$. The power spectrum is then fed into N-GenIC, the initial condition generator associated with Gadget-2.

[1] http://www.mpa-garching.mpg.de/gadget/
[2] http://camb.info/

Snapshot cubes are recorded at redshifts corresponding to every ~ 80 Mpc (comoving).

To create mock shear maps, we next perform ray-tracing. We divide each 3D box into three parallel pieces and project each slice onto a 2D plane perpendicular to the observer's line of sight, using the triangular shaped cloud scheme [58]. We then convert the surface density to the gravitational potential at each plane using Poisson's equation. At each position of the 4.2 million observed CFHTLenS galaxies, we follow a light ray from $z = 0$, traveling backward through the projection planes to the redshift of the galaxy, z_{gal}. For simplicity, we chose z_{gal} to be the peak of the photometric redshift probability distribution function (PDF). Using the most probable redshift, instead of the full PDF, can potentially induce biases as the former does not follow the stacked posterior probabilities when fainter galaxies are included (see Fig. 10 in Ref. [46]). We test this effect by ray-tracing to redshifts randomly drawn from the PDF of individual galaxies for one cosmology, and found the deviation of cosmological parameters in the full likelihood analysis to be negligible. Ref. [37] also found the bias caused by using the most probable photometric redshift to be small ($\Delta w_0 \approx 0.1$), but important for future, larger surveys.

The deflection angle, convergence, and shear are calculated at each plane for each light ray. Between the planes, the light rays travel in straight lines. Finally, for each cosmological model, we create 1,000 realizations (including κ and $\boldsymbol{\gamma}$ for each galaxy) by randomly rotating/shifting the simulation data cubes.

In total, we created 1,183,000 mock catalogues (91 models $\times$ 13 subfields per model $\times$ 1,000 realizations per subfield).

	Ω_m	w	σ_8				
1	0.624	-2.757	0.327	46	0.361	-0.606	0.171
2	0.849	-0.183	0.821	47	0.389	-0.939	0.454
3	0.136	-2.484	1.034	48	0.634	-1.575	0.976
4	0.295	-1.878	0.1	49	0.305	-0.879	0.765
5	0.418	-1.758	0.383	50	0.211	-0.333	0.341
6	0.615	-1.668	0.185	51	0.812	-1.788	0.722
7	0.558	-2.577	1.146	52	0.661	-0.486	0.892
8	0.915	-2.544	1.175	53	0.681	-2.97	0.61
9	0.7	-0.273	0.283	54	0.746	-0.09	1.118
10	0.446	-1.212	1.486	55	0.464	-2.121	0.906
11	0.991	-1.908	1.02	56	0.568	-0.516	1.331
12	0.155	-0.393	0.652	57	0.737	-2.847	1.203
13	0.145	-2.211	1.303	58	0.427	-2.91	0.411
14	0.981	-1.242	1.048	59	0.249	-2.727	0.369
15	0.409	-2.94	0.737	60	0.652	-1.029	1.458
16	0.436	-0.06	0.878	61	0.794	-1.365	0.156
17	0.183	-0.909	0.269	62	0.925	-0.636	1.259
18	0.502	-1.152	1.189	63	0.164	-2.181	0.313
19	0.38	-2.424	0.199	64	0.267	-2.667	1.317
20	0.887	-0.363	0.439	65	0.192	-1.605	1.401
21	0.276	-0.849	1.429	66	0.324	-2.001	1.217
22	0.718	-1.728	1.472	67	0.577	-3.0	0.948
23	0.755	-0.456	1.359	68	0.596	-0.696	0.496
24	0.831	-0.759	0.213	69	0.728	-0.12	0.596
25	0.455	-2.637	1.373	70	0.173	-0.423	1.231
26	0.671	-2.364	0.793	71	0.803	-2.607	0.255
27	0.765	-2.091	1.076	72	0.53	0.0	0.624
28	0.493	-0.243	0.297	73	0.69	-1.332	0.482
29	0.483	-1.515	0.68	74	0.549	-1.818	1.287
30	0.474	-1.302	0.114	75	0.239	-1.848	0.962
31	0.84	-2.274	1.387	76	0.906	-1.698	1.273
32	0.963	-2.151	0.51	77	0.512	-0.819	0.849
33	0.258	-1.395	0.241	78	0.399	-1.938	1.5
34	0.972	-0.666	0.694	79	0.37	-0.303	1.345
35	0.943	-2.394	0.835	80	0.869	-2.031	0.227
36	0.643	-2.454	1.444	81	0.709	-2.061	0.425
37	0.821	-2.88	0.863	82	0.286	-1.272	1.104
38	0.775	-1.122	1.132	83	0.784	-1.062	0.779
39	0.54	-0.03	1.161	84	0.342	-2.817	1.062
40	0.352	-0.576	1.09	85	1.0	-1.425	0.708
41	0.333	-0.213	0.552	86	0.878	-2.697	0.524
42	0.897	-0.999	0.468	87	0.606	-0.789	0.142
43	0.221	-1.485	0.666	88	0.521	-2.334	0.538
44	0.953	-1.545	0.355	89	0.587	-2.304	0.128
45	0.315	-2.241	0.638	90	0.201	-2.787	0.807
				91	0.859	-1.182	1.415

TABLE I. Cosmological parameters used in our simulations. The universe is assumed to be spatially flat ($\Omega_\Lambda + \Omega_m = 1$), with the Hubble constant $h = 0.72$, baryon density $\Omega_b h^2 = 0.0227$ and spectral index $n_s = 0.96$.

B. Convergence Maps

Next, we process the simulation catalogues, mimicking as closely as possible the procedures applied to the real CFHTLenS data. The transformation from intrinsic to observed galaxy ellipticity is [59],

$$\boldsymbol{e} = \begin{cases} \frac{\boldsymbol{e}_{\rm int}+\boldsymbol{g}}{1+\boldsymbol{g}^*\boldsymbol{e}_{\rm int}} & |\boldsymbol{g}| \leq 1 \\ \frac{1+\boldsymbol{g}\boldsymbol{e}^*_{\rm int}}{\boldsymbol{e}^*_{\rm int}+\boldsymbol{g}^*} & |\boldsymbol{g}| > 1 \end{cases} \tag{12}$$

$$\boldsymbol{g} = \frac{\boldsymbol{\gamma}}{1-\kappa}, \tag{13}$$

where $\boldsymbol{e}_{\rm int}$ is the galaxy's intrinsic ellipticity. For each simulated galaxy, we assign an intrinsic ellipticity by rotating the observed ellipticity for that galaxy by a random angle on the sky, while conserving its magnitude $|\boldsymbol{e}|$. $\boldsymbol{g} = g_1 + ig_2$ is the reduced shear, and asterisk denotes complex conjugation. To be consistent with the CFHTLenS analysis, we adopt the weak lensing limit ($|\boldsymbol{\gamma}| \ll 1$, $\kappa \ll 1$), hence $\boldsymbol{g} \approx \boldsymbol{\gamma}$, $\boldsymbol{e} \approx \boldsymbol{e}_{\rm int} + \boldsymbol{\gamma}$. We estimate the bias on cosmological parameters to be $< 50\%$ of the one σ error for σ_8, and $< 30\%$ for Ω_m, using results from Ref. [60] for a CFHTLenS-like survey (with $n_{gal} = 9.3$ arcmin^{-2} and sky coverage $f_{\rm sky} = 0.03$). We also add multiplicative noise by replacing $\boldsymbol{\gamma} \to \boldsymbol{\gamma}(1+m)$. As with CFHTLenS data, we continue with smoothing (eq. 4), convergence map construction (Eq. 11), masking (§ II B), and computing the power spectrum and peak counts (§ II C).

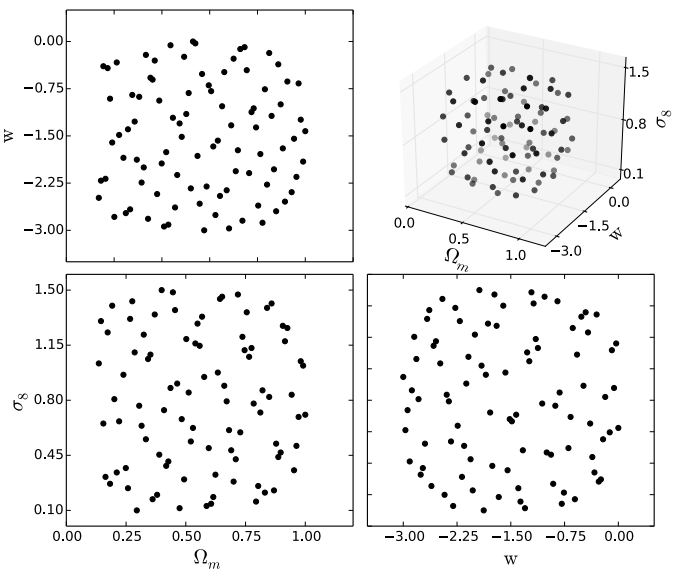

FIG. 2. Visual representation of the cosmological parameters in the 91 models used in our simulations, and listed in Table I.

C. Interpolation

We test two methods to interpolate from the 91 measured power spectra and peak counts to other cosmologicial models: (1) multi-dimensional *Radial Basis Function* (RBF) and (2) *Gaussian Process* (GP). RBF uses the average power spectrum or the peak counts (over 1,000 realizations) at each sampled point. The interpolated value is the weighted average of all sampling points, and the weight is a function of the distance from the interpolation point. We choose the function to be "multiquadric" ($\sqrt{(p_i/\epsilon)^2+1}$, where $p_i = |\boldsymbol{p}_i - \boldsymbol{p}_0|$ is the distance in parameter space, and ϵ is a constant chosen to be the average distance between sampling points), as it gives us the best results among other commonly used functions[3]. RBF interpolation is computed using scipy[4]. The GP method is a technique to interpolate smooth functions on an irregular grid, minimizing artifacts due to clustering of sampled points in parameter space. GP utilizes not only the mean value at each point, but also the standard deviation among the simulated realizations. We compute GP interpolation using the scikit-learn package[5].

Though GP uses more information than RBF, we do not find a significant difference between the two algorithms. We test the validity of both interpolators as follows. First, we choose one model as the test point, and use the remaining 90 models to construct the interpolator. We then compare the prediction at the test point to the actual power spectrum and peak counts. This is repeated 91 times for all models. For both power spectrum and peak counts, using either RBF or GP, we are able to predict at $\sim 1\%$ level for the power spectrum (with only one case that is over 5%) and at $\sim 5\%$ level for peak counts (with few cases that are slightly larger than 5% for high κ peaks). Most our predictions are well within the error bars (i.e. the variance between realizations). The interpolation performance decreases slightly at the edges of the model parameter space. Fig. 3 shows a typical example of the interpolated power spectrum and peak counts, compared against the actual values. In our final analysis, we use RBF for faster computation.

D. Parameter Estimation

With only three free parameters, we can directly compute the probability distribution on a 3D parameter grid. According to Bayes' theorem, the posterior probability of a set of parameters $\boldsymbol{p} = [\Omega_m, w, \sigma_8]$ for given data $\boldsymbol{d} = [d_1, d_2, ...d_n]$ is,

$$P(\boldsymbol{p}|\boldsymbol{d}) = \frac{P(\boldsymbol{p})P(\boldsymbol{d}|\boldsymbol{p})}{P(\boldsymbol{d})}, \tag{14}$$

where $P(\boldsymbol{p})$ is the prior, $P(\boldsymbol{d}|\boldsymbol{p})$ the likelihood function of measuring $\boldsymbol{d}$ given $\boldsymbol{p}$, and $P(\boldsymbol{d})$ the normalization. Under the assumption that the observables are Gaussian distributed, the likelihood function is,

$$P(\boldsymbol{d}|\boldsymbol{p}) = \frac{1}{(2\pi)^{n/2}|\mathbf{C}|^{1/2}} \times \exp\left[-0.5(\boldsymbol{d}-\boldsymbol{\mu})\mathbf{C}^{-1}(\boldsymbol{d}-\boldsymbol{\mu})\right], \tag{15}$$

where $\boldsymbol{\mu}$ is the prediction as described in § III C, n is the number of free parameters (= 3 in this work), and $\mathbf{C}$ the (constant) covariance matrix. We compute $\mathbf{C}$ using a fiducial model $[\Omega_m, w, \sigma_8] = [0.305, -0.879, 0.765]$, assuming $d\mathbf{C}/d\boldsymbol{p}$ is small. The fiducial model is selected from the 91 models so that its parameters are close to the WMAP7 values [61]. We use a flat prior for Ω_m in $[0, 0.8]$, w in $[-2.1, -0.3]$, and σ_8 in $[0.1, 1.4]$. We obtain the normalization $P(\boldsymbol{d})$ by setting the sum of the probability of all grid points to unity. Within the range of our flat priors, we compute $P(\boldsymbol{p}|\boldsymbol{d})$ for 100^3 equally spaced grid points. To obtain 2D error contours, we marginalize over the third parameter. The results are presented in § IV below.

[3] For example, "inverse": $1/\sqrt{(p/\epsilon)^2+1}$, "Gaussian": $\exp[-(p/\epsilon)^2]$, "linear": p, "cubic": p^3, and "quintic": p^5.

[4] `http://www.scipy.org`

[5] `http://scikit-learn.org`

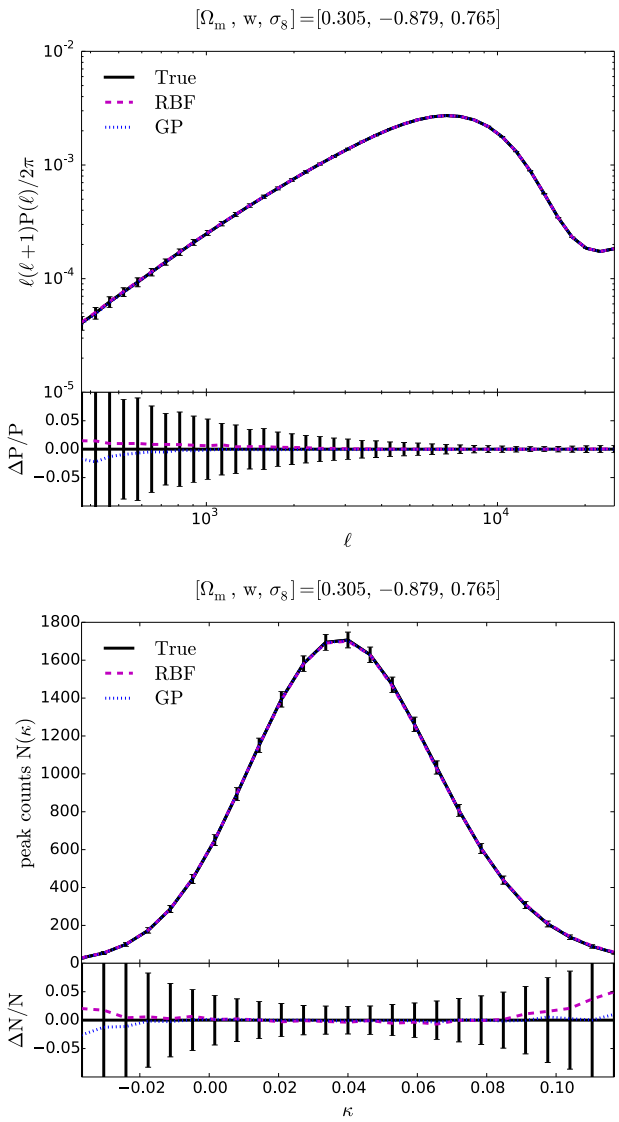

FIG. 3. Examples of the interpolated power spectrum (upper panel) with 0.5 arcmin smoothing and peak counts (lower panel) with 1.0 arcmin smoothing and 25 κ bins, using the two different interpolation techniques *Radial Basis Function* (RBF) and *Gaussian Process* (GP). The solid curves show the true quantities for the given cosmological model (#49 in Table I), and the dashed and dotted curves show the interpolations based on the other 90 models.

IV. RESULTS

A. Power Spectrum

We first compare our power spectrum model with theoretical predictions. Fig. 4 shows the interpolated power for $\ell = 3,000$ (7.2 arcmin) as a function of Ω_m, w, and σ_8. We only show the change for one particular ℓ, because the change is similar for all scales within our model ($370 < \ell < 25,000$). The upper panel of Fig. 4 is from our simulations, and the lower panel is computed using fitting formulae from [62] and the code Nicaea[6]. The third parameter for each plane is at a fixed value ($[\Omega_m, w, \sigma_8] = [0.26, -1.0, 0.8]$). Overall, simulations and theory predictions are in good agreement, with the figure showing that the power in the upper and lower panels is similar, and varies as a function of cosmological parameters similarly. For a more quantitative test of the power spectrum, see Fig. 1 in Ref. [27]. For cosmological constraints, we use our simulated power spectra directly, rather than theoretical fitting formulae. The up-turn seen at $\ell > 20,000$ is an artifact due to our map resolution. However, we found no bias from this artifact, when comparing error contours using bins with $\ell < 20,000$ and all available bins (up to $\ell = 25,000$).

Reference [47] identified 25% of the 172 individual CFHTLenS pointings, each ≈ 1 deg^2 in size, with significant PSF residuals. Including these fields can increase the systematic error in the 2PCF, and possibly impact other statistics. However, because the power spectrum is a convolution of the signal and the mask, it is susceptible to the masking pattern (due to bright stars and bad pixels) whose characteristic scale is significantly larger than the smoothing scale. As each bad field removes one square degree from the data, much larger than our $\sim$ arcmin smoothing scale, excluding these areas can also introduce additional noise. To study the effect due to PSF residuals and masks, we compute the power spectrum for all fields and for the 75% "pass" fields, shown in the upper panel of Fig. 5. We find power spectra with or without this PSF screening are consistent within errors on large scales. On small scales ($\ell > 7,000$, or 3 arcmin), however, we find a significant difference in power spectra with or without the corrupted fields. This difference is caused primarily by the particular masking pattern, rather than field selections. This is demonstrated by performing the same comparison using our simulated power spectra, with the same corrupted regions either included or excluded. The result of this comparison is shown (for the fiducial cosmology) in the lower panel of Fig. 5, revealing a similarly large discrepancy for $\ell > 7,000$.

Fig. 6 shows the 68% confidence level (CL) error contour in the Ω_m–σ_8 plane (marginalized over w) for the full set and for the pass–only fields, and for all available ℓ and for $\ell < 7,000$. We found the contours are fairly consistent among the four cases. To be conservative, we use the 75% pass fields only for our power spectrum analysis, and further limit our analysis to $\ell < 7,000$. The latter restriction eliminates small scales, where baryonic effects can bias the shear correlation function by more than 5-10% [63], and lead to a non-negligible bias on the best-constrained cosmological parameter combination Σ_8 (defined below). For all four contours in the figure, we are unable to exclude the lower right corner in the Ω_m–σ_8 plane. Given the strong degeneracy between Ω_m and σ_8,

[6] http://www2.iap.fr/users/kilbinge/nicaea/

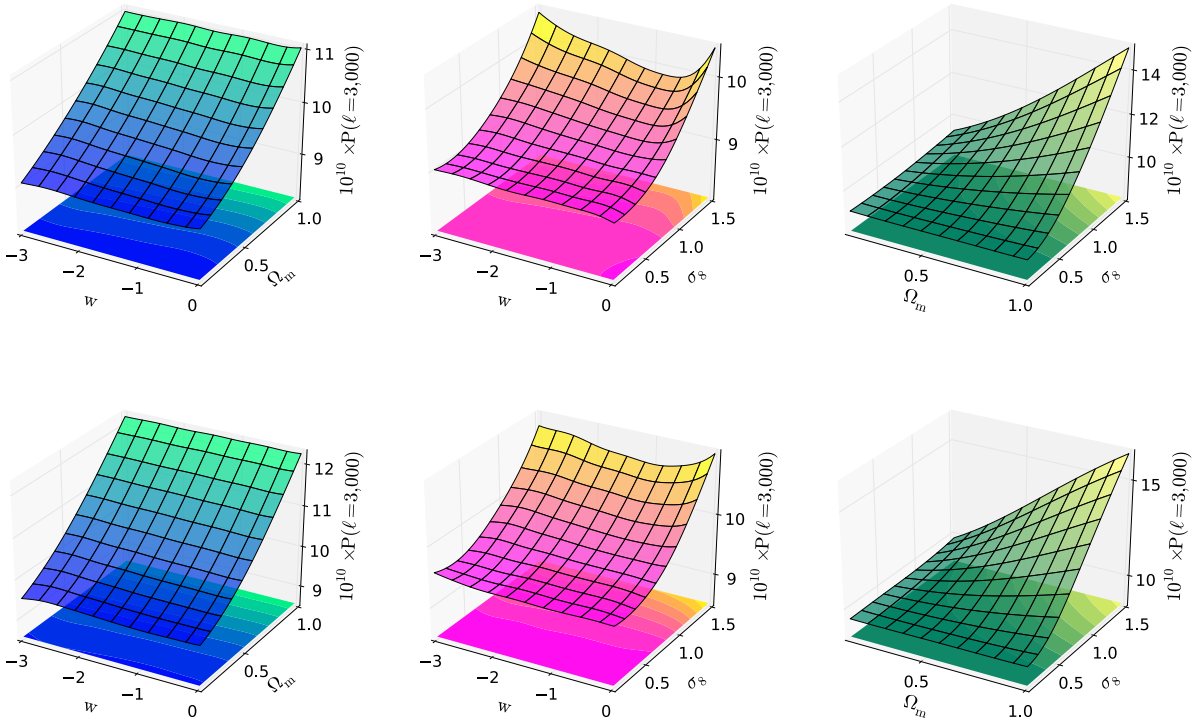

FIG. 4. Interpolated power for $\ell = 3,000$ (7.2 arcmin) as a function of Ω_m, w, and σ_8 using simulations (upper panel) and fitting formula from Ref. [62] (lower panel). The third parameter for each plane is at a fixed value ($[\Omega_m, w, \sigma_8] = [0.26, -1.0, 0.8]$).

it is of little meaning to quote a best fit for individual parameters; rather we will compare the areas of the 2D contours for various probes, and obtain constraints on a combination of the two parameters (see below).

B. Peak Counts

Interpolated peak counts from simulations as a function of cosmological parameters are shown in Fig. 7. We present the effect for three representative κ values, low ($< 1\sigma_\kappa$, upper panel), medium ($1 - 3\sigma_\kappa$, middle panel), and high ($> 3\sigma_\kappa$, lower panel), where $\sigma_\kappa = 0.03$ is the standard deviation in the convergence map for 1 arcmin smoothing (with galaxy noise). As in Fig. 4, the third parameter for each plane is at a fixed value ($[\Omega_m, w, \sigma_8] = [0.26, -1.0, 0.8]$). Low and high peaks behave similarly, where larger Ω_m or σ_8 increases the number of peaks. Medium peaks behave the opposite way. Ref. [27] investigated the origin of peaks, and found typical high peaks are linked to one single massive halo, while medium peaks are associated with constellations of 4–8 lower-mass, off-center halos near the line of sight. It is not surprising to see the effect of Ω_m and σ_8 on high peaks, as higher values increase the number of massive halos. The opposite behavior of medium peaks is somewhat counter-intuitive, but has been observed and explained in [27].

As peak counts are local, we expect field selections to have a smaller impact on them, beyond modifying the total number of peaks and their variance. This is shown to be the case in Fig. 8, where we compare peak counts from pass–only fields and from all fields, and found these to be consistent for all κ within errors (for a fair comparison, peak counts using all fields are multiplied by the sky ratio of pass fields to all fields, ≈ 0.75). Therefore, unlike for the power spectrum, we choose to include all fields for peak counts for tighter constraints.

We test the constraints from different smoothing scales. Large smoothing windows reduce the total number of peaks, and wash out cosmological information, whereas small smoothing scales result in very noisy distributions. We examine six smoothing scales (0.5, 1.0, 1.8, 3.5, 5.3, and 8.9 arcmin). The smallest (0.5 arcmin) and the largest (8.9 arcmin) yield significantly larger errors than the other four. We show the error contours from these four, intermediate smoothing scales in Fig. 9. The 1.0 and 1.8 arcmin scales yield tighter contours than the other two, larger scales. A combination of these two best scales (also shown in the figure) further tighten the errors, and we therefore use it in our final analysis. Clearly, the above is only a limited investigation of the benefit of

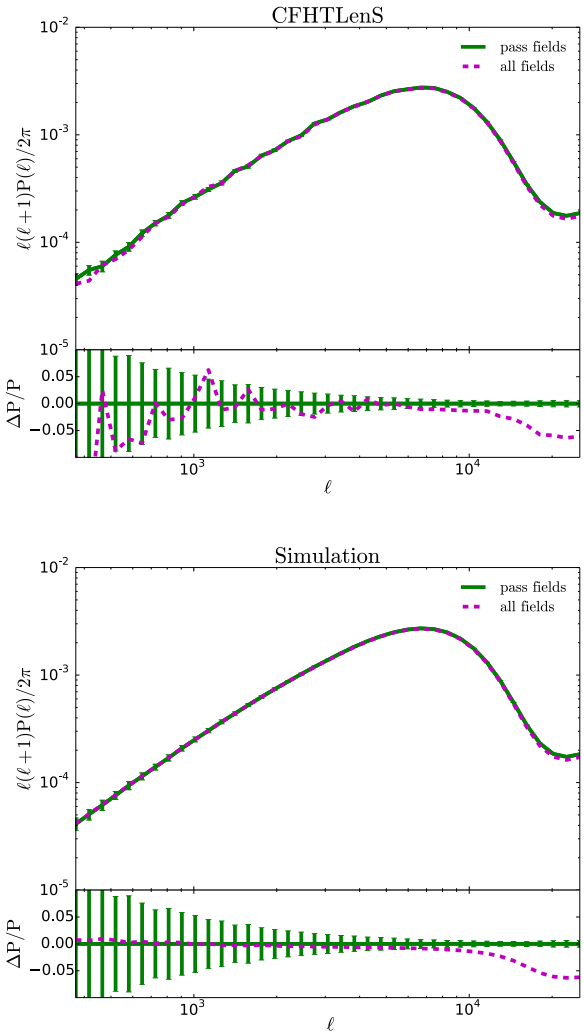

FIG. 5. Comparison of the CFHTLenS (top panel) and simulated (bottom panel) power spectrum measured using 75% of the fields (solid line) which pass the PSF residual test and all fields (dashed line). The error is measured from our simulations.

using multiple smoothing scales. We expect that a more rigorous study in the future, identifying optimal filter shapes, sizes, and combinations can help further tighten constraints from peak counts.

C. Cosmological Constraints

From the interpolated planes for the power spectrum (Fig. 4) and peak counts (Fig. 7), we see some similarity between the two statistics. They both suffer a similar Ω_m–σ_8 degeneracy, and both have a much weaker dependence on w than on Ω_m or σ_8. However, peak counts are less impacted than the power spectrum by field selections (due to PSF residuals) and masks, two non-trivial

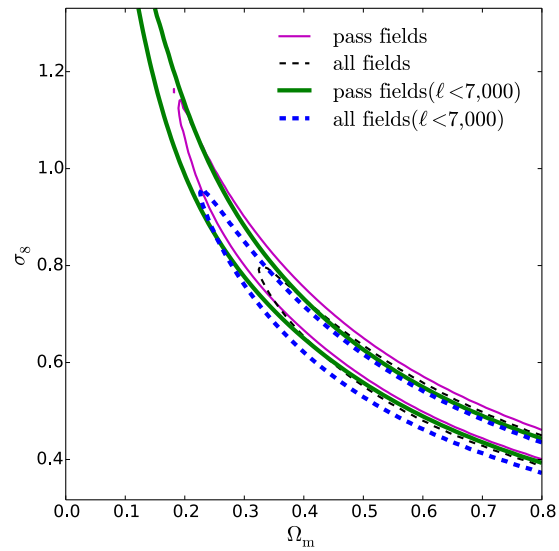

FIG. 6. 68% error contours from the power spectrum measured using only the 75% of the CFHTLenS fields that pass the PSF residual test (solid curves) and for all fields (dashed curves). Constraints are shown with (thick curves) and without (thin curves) imposing an upper limit $\ell < 7,000$.

systematics in CFHTLenS observations.

Fig. 11 shows 68% and 95% confidence contours for the power spectrum, peak counts (1.0 + 1.8 arcmin), and the combination of both statistics. The full covariance is taken into account when combining the two statistics. Table II lists the marginalized constraints on $\Sigma_8 = \sigma_8(\Omega_m/0.27)^\alpha$, which is roughly orthogonal to the Ω_m–σ_8 degeneracy direction. We find the best fit $\alpha = 0.63$ and $\Sigma_8 = 0.85^{+0.03}_{-0.03}$ (with a fixed α). For comparison, using the 2PCF, Ref. [8] found this constraint (with best fit $\alpha = 0.59$) to be $0.79^{+0.07}_{-0.06}$, comparable to within $\approx 1\sigma$ with our result (although their values have been marginalized over additional cosmological parameters). Our probability distribution for Σ_8 (Fig. 10) also shows a somewhat asymmetric shape, with a long tail to low values, when using the power spectrum, which creates our asymmetric error bars.

The relative area covered by each contour is listed in Table III, normalized by the size of the 68% contour from the power spectrum. In both 2D parameter planes shown, the constraints from the peak counts is stronger than from the power spectrum, and largely determines the size and shape of the combined contour. The size of this combined contour is a factor of $\approx 1.5 - 2$ smaller than from the power spectrum alone. One may worry that this result is unfair, as our power spectrum analysis uses only 75% of all fields and is restricted to $\ell < 7,000$, while peak counts use all fields and include information from smoothing scales as small as 1 arcmin. We find that using all fields can reduce the power spectrum error

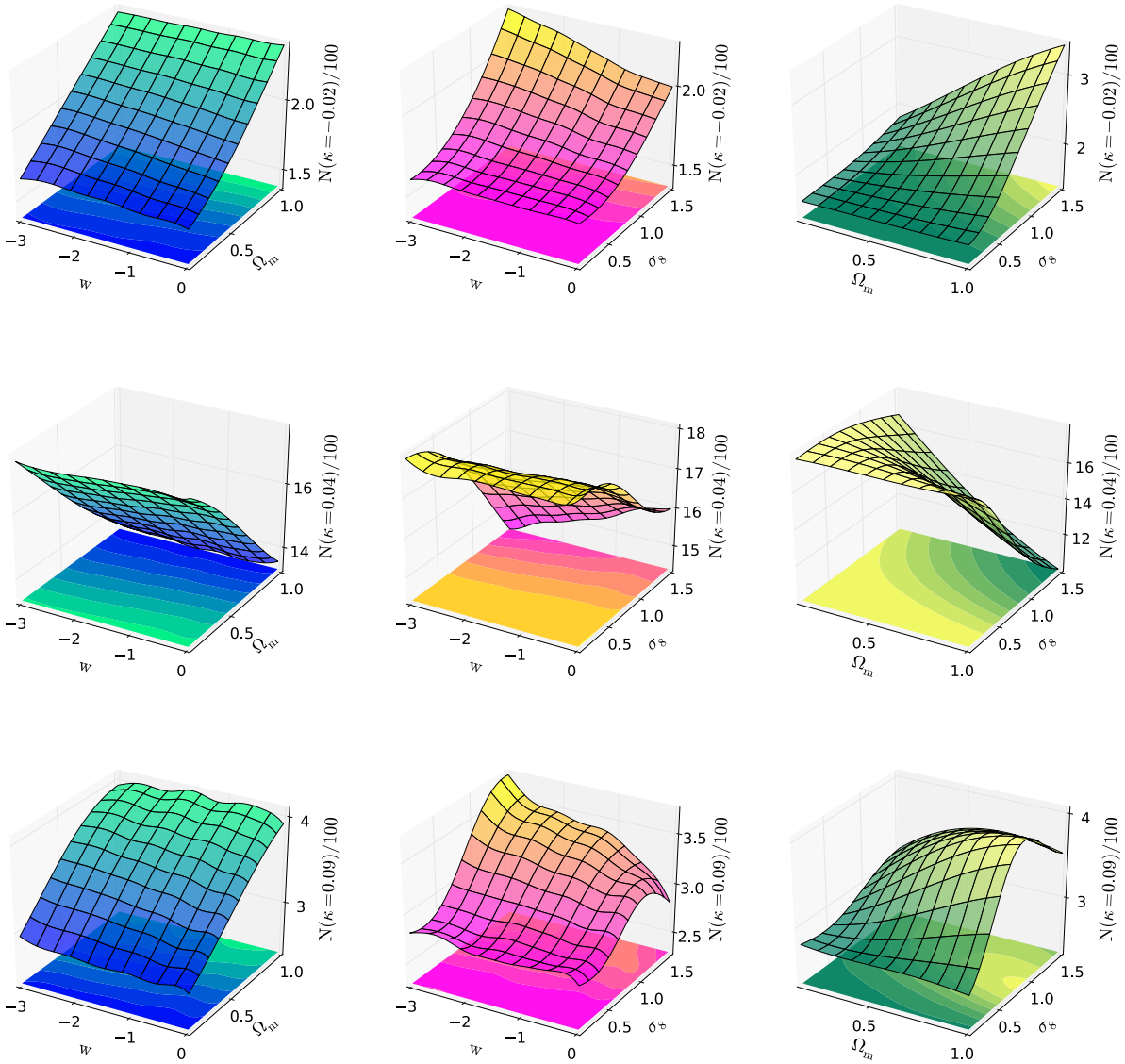

FIG. 7. Interpolated number counts for typical low ($< 1\sigma_\kappa$, top panel), medium ($1-3\sigma_\kappa$, middle panel), and high ($> 3\sigma_\kappa$, bottom panel) peaks, where $\sigma_\kappa = 0.03$ is the standard deviation of κ measured in our simulations. As in Fig. 4, the third parameter in each panel is at a fixed value ($[\Omega_m, w, \sigma_8] = [0.26, -1.0, 0.8]$).

contour by 83%, while using all available ℓ can reduce the contour by 90%. When both of these restrictions on the power spectrum are lifted, the area enclosed by the 68% confidence level contour from the power spectrum is 62% smaller than that listed in Table III, making the power–spectrum–alone and the peaks–alone constraints comparable. However, as argued above, the power spectrum result in this case may be significantly biased by systematic errors and baryonic effects (and, as shown by the blue curve in Fig. 6, the concordance ΛCDM model is indeed outside the 68% CL in this case).

Ref. [67] examined the covariance between cluster counts and weak lensing power spectrum and found that including the cross-covariance leads to degradation of cosmological constraints by few percent (also see Ref. [68]). We test the importance of the covariance between peak counts and the power spectrum. Fig. 12 shows the total covariance of the power spectrum and peak counts (1.0 + 1.8 arcmin smoothing scales). Fig. 13 shows the error contours when such cross-covariance is included in the analysis (as done throughout our paper; black solid curves) or ignored (dashed red curves). In the latter case, i.e. when the two statistics are assumed to be independent, the area of the 68% CL contour is

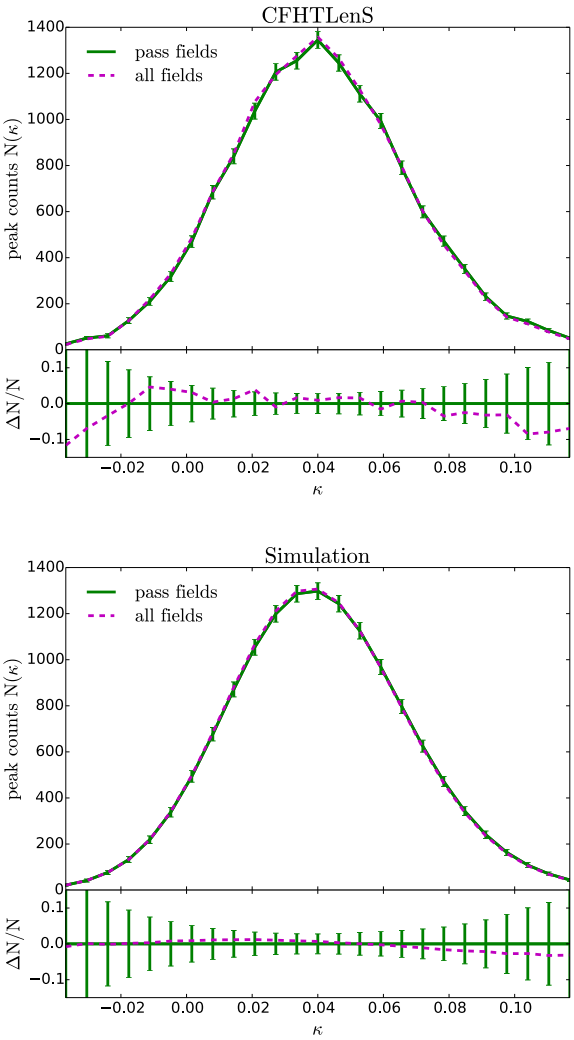

FIG. 8. Comparison of the CFHTLenS (upper panel) and simulated (lower panel) peak counts measured using 75% of the fields (solid curves) which pass the PSF residual test and all fields (dashed curves). The error is measured from our simulations.

reduced by $\approx 16\%$, a somewhat larger change than was found for the combination of cluster counts and power spectrum (although for different parameters; see Fig.12 in Ref. [67]).

Finally, we show in Fig. 14 the best–fit and two other models, randomly selected from within the 68% error banana, along with the CFHTLenS power spectrum and peaks. The reduced $\chi^2 \approx 2$ for the best–fit model to the power spectrum is large, indicating the model does not fully describe the data, and the discrimination between the best-fit model and other models located along the ridge of the degeneracy "banana" is weak. Overall, these results indicate that there may still be significant systematic errors, even after the problematic fields have been excluded. The reduced $\chi^2 \approx 0.8$ for the fits to the peak counts is significantly lower.

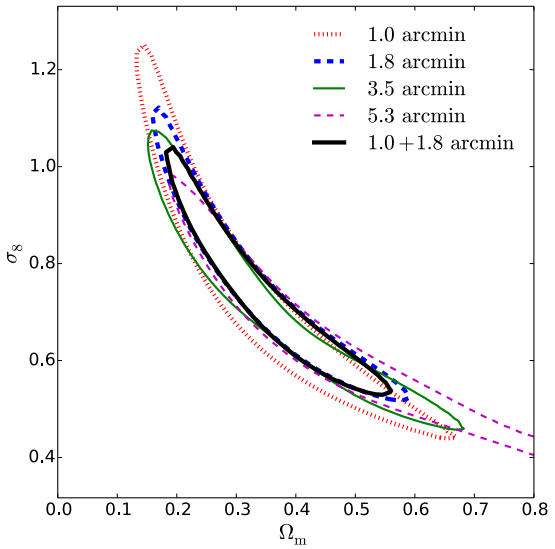

FIG. 9. 68% error contours from peak counts using smoothing scales of 1.0 (dotted curve), 1.8 (thick dashed curve), 3.5 (thin solid curve), and 5.3 (thin dashed curve) arcmin, as well as from peak counts with 1.0 and 1.8 arcmin smoothing scales in combination (thick solid curve).

	Σ_8	α
power spectrum	$0.87^{+0.05}_{-0.06}$	0.64
peak counts	$0.84^{+0.03}_{-0.04}$	0.60
combined	$0.85^{+0.03}_{-0.03}$	0.63

TABLE II. Marginalized 68% constraints for $\Sigma_8 = \sigma_8(\Omega_m/0.27)^\alpha$, using the power spectrum, peak counts, and their combination.

V. CONCLUSIONS

In this paper, we have run 91 cosmological models, built a CFHTLenS–specific weak lensing emulator for the power spectrum and peak counts, and obtained constraints on Ω_m, w, and σ_8. Peak counts as a recently

	w–Ω_m		Ω_m–σ_8	
	68%	95%	68%	95%
power spectrum	1.00	1.74	1.00	1.99
peak counts	0.41	1.01	0.59	1.51
combined	0.42	1.05	0.61	1.46

TABLE III. The areas of the two-dimensional error contours computed using the power spectrum, peak counts, and their combination, in two parameter planes (marginalized over the third parameter). The areas are normalized to the 68% power spectrum contour in each case.

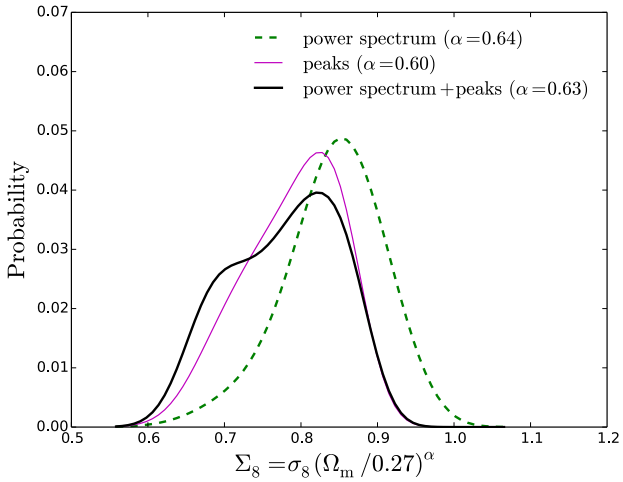

FIG. 10. Constraints on the parameter $\Sigma_8 = \sigma_8(\Omega_m/0.27)^\alpha$, using the power spectrum (dashed line), peak counts (thin solid line), and their combination (thick solid line). The power spectrum is computed using the 75% of the fields that pass the PSF residual test, and restrictd to $\ell < 7,000$. Peak counts are computed using all fields, and include measurements of peaks on two smoothing scales (1.0 and 1.8 arcmin).

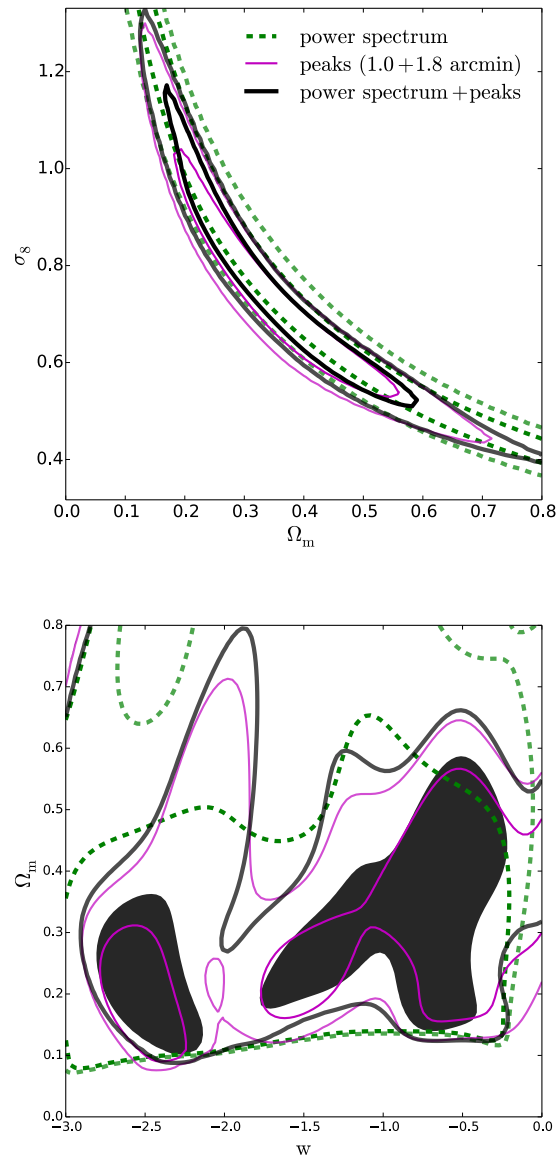

FIG. 11. 68% (dark color) and 95% (light color) error contours from the power spectrum (dashed curves), peak counts (thin solid curves), and their combination (thick solid curves). The shaded region in the bottom panel is the 68% error contour for the combination. The power spectrum is computed using the 75% of the fields that pass the PSF residual test, and restricted to $\ell < 7,000$. Peak counts are computed using all fields, and include measurements of peaks on two smoothing scales (1.0 and 1.8 arcmin).

developed non-Gaussian statistics have previously been proven in theory to have comparable constraining power as the power spectrum. This work is the first attempt to test this hypothesis rigorously on real data.

We have found that combining peak counts with the power spectrum can reduce the area of the 2D error contour by a factor of ≈ 2 compared to using the power spectrum alone. Combining both statistics, we obtained $\sigma_8(\Omega_m/0.27)^{0.63} = 0.85^{+0.03}_{-0.03}$.

To conclude, peak counts can serve as a complementary probe to the power spectrum in two important ways:

(1) As a calibration tool for systematics. Peaks with small ($\sim$ arcmin) smoothing scales suffer less (or are impacted differently by) systematics than the power spectrum. For CFHTLenS, we have found that the PSF residuals have little impact on peak counts, in contrast with the bias seen with the 2PCF in Ref. [47]. We find that masking also has little impact on the peak counts, whereas it changes the power spectrum at small scales ($\ell > 7,000$). The change in the power spectrum does not impact cosmological constraints, as long as the mask is taken into consideration in the model (e.g. Fig. 6). Furthermore, in our previous work on theoretical systematics due to the magnification bias [54], we also discovered that, while both the power spectrum and peak counts are affected, the resulting directions of the biases in the cosmology parameter space are different. Combining the two probes can mitigate the impact from these systematics.

(2) By providing tighter constraints on cosmological parameters. The peak counts by themselves have a similar, or even better constraining power than the power spectrum. This can be attributed to the fact that the peaks capture information from non-Gaussian features of the convergence maps. We have shown in Fig. 11 and Table III that combining power spectrum and peak counts improves the constraints by a factor of $\approx$ two, compared

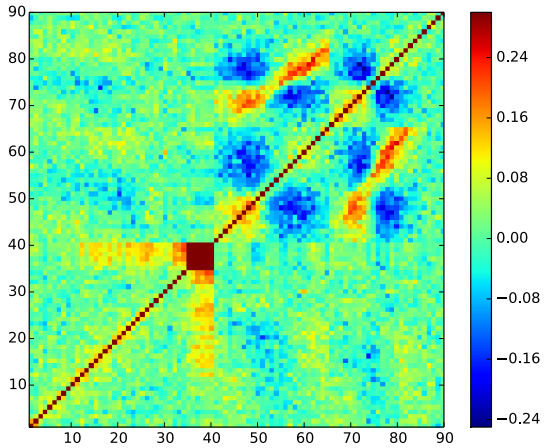

FIG. 12. Correlation coefficients of the total covariance. Bins 1 - 40 are for the power spectrum, bin 41 - 65 are for peak counts with 1.0 arcmin smoothing scale, and bins 66 - 90 are for peak counts with 1.8 arcmin smoothing scale.

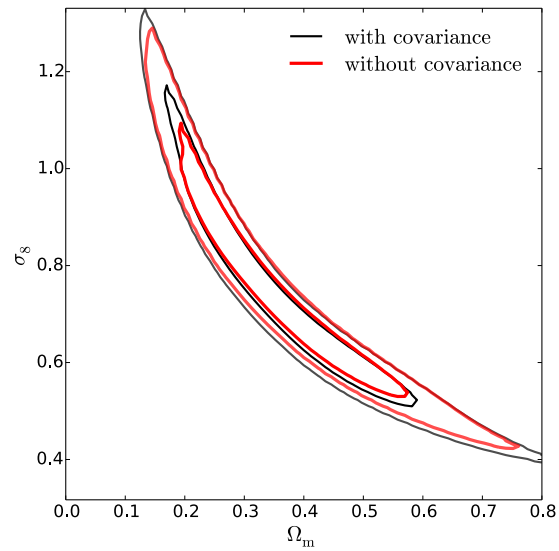

FIG. 13. 68% (dark color) and 95% (light color) power spectrum + peak counts error contours with (thin curves) and without (thick curves) the cross-covariance. The power spectrum is computed using the 75% of the fields that pass the PSF residual test, and restricted to $\ell < 7,000$. Peak counts are computed using all fields, and include measurements of peaks on two smoothing scales (1.0 and 1.8 arcmin).

to using the power spectrum alone.

The potential of the peak counts have not yet been fully realized. Our work can be improved further by:

(1) Examining the effects of additional smoothing scales, binning of peaks, and the robustness of the results under masking. We have examined only six smoothing scales, and demonstrated that using multiple smoothing scales can reduce the size of the area of the error contour by a moderate amount. We also showed that masking can change the power spectrum. More detailed study on these effects can be beneficial.

(2) Including the cosmological dependence of the covariance matrix, especially for peak counts. We use a constant covariance matrix in this work, assuming the cosmological dependence is weak, as we expect the covariance to be dominated by the shape noise. However, as the survey size increases, cosmological sensitivity should be taken into consideration when constructing the covariance matrix.

(3) Increasing the number of independent simulations run for each cosmological model. In our current work, due to computational limitations, we have only used one independent N-body simulation per model. Although we randomly rotate and shift the lensing planes to create multiple pseudo-independent realizations, some outliers (such as massive halos) will inevitably be repeated in several maps. However, our previous work has shown that the bulk of the cosmological information from peak counts resides in low-amplitude peaks, which do not arise from single massive halos; these peaks should be less susceptible to repeated structures between pseudo-random realizations. Nevertheless, to test possible errors due to not having sufficiently independent maps, we ran a separate set of 50 simulations for one cosmology. We found that the variance in the (noiseless) power spectrum and peak counts is increased by approximately 10%, when compared to that using only one simulation. However, when noise is added, the difference is no longer systematic, with a 5% fluctuation and is consistent with 0. We also found a larger-than Gaussian variance even at our lowest $\ell = 400$, by approximately 10%. This increase in the variance due to non-Gaussianities is somewhat lower than that found previously [69]. Further details on tests of the covariance matrices will be presented in our companion paper (Petri et al., in prep).

Future WL surveys, such as the Dark Energy Survey, and the Large Synoptic Survey Telescope, cover much larger areas (5,000 and 20,000 deg^2, respectively), hence are more sensitive to instrumental and theoretical systematics. These will need to be addressed carefully in order to realize the full potential of these larger surveys.

ACKNOWLEDGMENTS

We thank Ludovic Van Waerbeke and Hendrik Hildebrandt for useful discussions. Simulations for this work were performed at the NSF Extreme Science and Engineering Discovery Environment (XSEDE), supported by grant number ACI-1053575, and at the New York Center for Computational Sciences, a cooperative effort between Brookhaven National Laboratory and Stony Brook Uni-

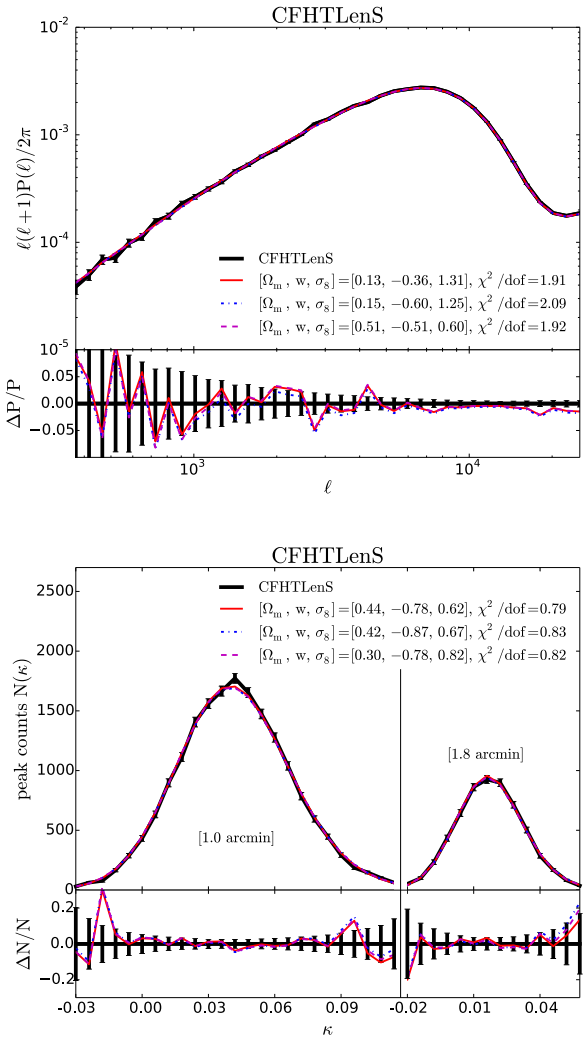

FIG. 14. Fits to the CFHTLenS (thick solid curves) power spectrum (upper panel) and peak counts (lower panel). The peak counts on 1.0 and 1.8 arcmin scales are concatenated on the x-axis. The best fits (thin solid curves) and two other models (dash-dotted and dashed curves) randomly selected from within the 68% error bananas, are shown for reference.

versity, supported in part by the State of New York. This work was supported in part by the U.S. Department of Energy under Contract No. DE-AC02-98CH10886 and Contract No. DE-SC0012704, and by the NSF grant AST-1210877 (to Z.H.).

[1] A. Refregier, ARA&A **41**, 645 (2003), [arXiv:arXiv:astro-ph/0307212].
[2] P. Schneider, ArXiv Astrophysics e-prints (2005), [arXiv:arXiv:astro-ph/0509252].
[3] H. Hoekstra and B. Jain, Annual Review of Nuclear and Particle Science **58**, 99 (2008), [arXiv:0805.0139].
[4] M. Bartelmann, Classical and Quantum Gravity **27**, 233001 (2010).
[5] D. H. Weinberg *et al.*, Phys. Rep. **530**, 87 (2013), [arXiv:1201.2434].
[6] T. Schrabback *et al.*, A&A **516**, A63 (2010), [arXiv:0911.0053].
[7] C. Heymans *et al.*, MNRAS **427**, 146 (2012), [arXiv:1210.0032].
[8] M. Kilbinger *et al.*, MNRAS **430**, 2200 (2013), [arXiv:1212.3338].
[9] F. Bernardeau, L. van Waerbeke and Y. Mellier, A&A **322**, 1 (1997), [arXiv:arXiv:astro-ph/9609122].
[10] B. Jain and U. Seljak, ApJ **484**, 560 (1997), [arXiv:arXiv:astro-ph/9611077].
[11] L. Hui, ApJL **519**, L9 (1999), [arXiv:arXiv:astro-ph/9902275].
[12] L. van Waerbeke, F. Bernardeau and Y. Mellier, A&A **342**, 15 (1999), [arXiv:astro-ph/9807007].
[13] B. Jain, U. Seljak and S. White, ApJ **530**, 547 (2000), [arXiv:arXiv:astro-ph/9901191].

[14] B. Jain and L. Van Waerbeke, ApJL **530**, L1 (2000), [arXiv:arXiv:astro-ph/9910459].
[15] L. Van Waerbeke, T. Hamana, R. Scoccimarro, S. Colombi and F. Bernardeau, MNRAS **322**, 918 (2001), [arXiv:astro-ph/0009426].
[16] M. Takada and B. Jain, MNRAS **337**, 875 (2002), [arXiv:arXiv:astro-ph/0205055].
[17] M. Takada and B. Jain, MNRAS **344**, 857 (2003), [arXiv:arXiv:astro-ph/0304034].
[18] M. Zaldarriaga and R. Scoccimarro, ApJ **584**, 559 (2003), [arXiv:arXiv:astro-ph/0208075].
[19] M. Takada and B. Jain, MNRAS **348**, 897 (2004), [arXiv:arXiv:astro-ph/0310125].
[20] S. Dodelson and P. Zhang, Phys. Rev. D**72**, 083001 (2005), [arXiv:arXiv:astro-ph/0501063].
[21] M. Kilbinger and P. Schneider, A&A **442**, 69 (2005), [arXiv:astro-ph/0505581].
[22] E. Sefusatti, M. Crocce, S. Pueblas and R. Scoccimarro, Phys. Rev. D**74**, 023522 (2006), [arXiv:arXiv:astro-ph/0604505].
[23] L. Marian, R. E. Smith and G. M. Bernstein, ApJL **698**, L33 (2009), [arXiv:0811.1991].
[24] J. Bergé, A. Amara and A. Réfrégier, ApJ **712**, 992 (2010), [arXiv:0909.0529].
[25] M. Maturi, C. Angrick, F. Pace and M. Bartelmann, A&A **519**, A23 (2010), [arXiv:0907.1849].
[26] S. Vafaei *et al.*, Astroparticle Physics **32**, 340 (2010), [arXiv:0905.3726].
[27] X. Yang *et al.*, Phys. Rev. D**84**, 043529 (2011), [arXiv:1109.6333].
[28] L. Marian, R. E. Smith, S. Hilbert and P. Schneider, MNRAS **432**, 1338 (2013), [arXiv:1301.5001].
[29] A. Petri, Z. Haiman, L. Hui, M. May and J. M. Kratochvil, Phys. Rev. D**88**, 123002 (2013), [arXiv:1309.4460].
[30] J. P. Dietrich and J. Hartlap, MNRAS **402**, 1049 (2010), [arXiv:0906.3512].
[31] J. M. Kratochvil, Z. Haiman and M. May, Phys. Rev. D**81**, 043519 (2010), [arXiv:0907.0486].
[32] L. Marian, S. Hilbert, R. E. Smith, P. Schneider and V. Desjacques, ApJL **728**, L13 (2011), [arXiv:1010.5242].
[33] L. Marian, R. E. Smith, S. Hilbert and P. Schneider, MNRAS **423**, 1711 (2012), [arXiv:1110.4635].
[34] X. Yang, J. M. Kratochvil, K. Huffenberger, Z. Haiman and M. May, Phys. Rev. D**87**, 023511 (2013), [arXiv:1210.0608].
[35] L. Fu *et al.*, MNRAS **441**, 2725 (2014), [arXiv:1404.5469].
[36] E. Semboloni *et al.*, MNRAS **410**, 143 (2011), [arXiv:1005.4941].
[37] M. Shirasaki and N. Yoshida, ApJ **786**, 43 (2014), [arXiv:1312.5032].
[38] L. Van Waerbeke *et al.*, MNRAS **433**, 3373 (2013), [arXiv:1303.1806].
[39] H. Shan *et al.*, ArXiv e-prints (2011), [arXiv:1108.1981].
[40] Z. Fan *et al.*, ArXiv e-prints (2010), [arXiv:1006.5121].
[41] K. Heitmann, M. White, C. Wagner, S. Habib and D. Higdon, ApJ **715**, 104 (2010), [arXiv:0812.1052].
[42] K. Heitmann *et al.*, ApJ **705**, 156 (2009), [arXiv:0902.0429].
[43] E. Lawrence *et al.*, ApJ **713**, 1322 (2010), [arXiv:0912.4490].
[44] K. Heitmann, E. Lawrence, J. Kwan, S. Habib and D. Higdon, ApJ **780**, 111 (2014), [arXiv:1304.7849].
[45] T. Erben *et al.*, MNRAS **433**, 2545 (2013), [arXiv:1210.8156].
[46] H. Hildebrandt *et al.*, MNRAS **421**, 2355 (2012), [arXiv:1111.4434].
[47] C. Heymans *et al.*, MNRAS **427**, 146 (2012), [arXiv:1210.0032].
[48] L. Miller *et al.*, MNRAS **429**, 2858 (2013), [arXiv:1210.8201].
[49] H. S. M. Coxeter, *Introduction to Geometry*, second ed. (Wiley, New York, NY, 1989).
[50] N. Kaiser and G. Squires, ApJ **404**, 441 (1993).
[51] J. T. VanderPlas, A. J. Connolly, B. Jain and M. Jarvis, ApJ **744**, 180 (2012), [arXiv:1109.5175].
[52] X. Liu, Q. Wang, C. Pan and Z. Fan, ApJ **784**, 31 (2014), [arXiv:1304.2873].
[53] D. Bard, J. M. Kratochvil and W. Dawson, ArXiv e-prints (2014), [arXiv:1410.5446].
[54] J. Liu, Z. Haiman, L. Hui, J. M. Kratochvil and M. May, Phys. Rev. D**89**, 023515 (2014).
[55] J. M. Kratochvil *et al.*, Phys. Rev. D**85**, 103513 (2012), [arXiv:1109.6334].
[56] D. Bard *et al.*, ApJ **774**, 49 (2013), [arXiv:1301.0830].
[57] A. Lewis, A. Challinor and A. Lasenby, ApJ **538**, 473 (2000), [arXiv:arXiv:astro-ph/9911177].
[58] R. Hockney and J. Eastwood, Chap **4**, 113 (1988).
[59] C. Seitz and P. Schneider, A&A **318**, 687 (1997), [arXiv:astro-ph/9601079].
[60] S. Dodelson, C. Shapiro and M. White, Phys. Rev. D**73**, 023009 (2006), [arXiv:arXiv:astro-ph/0508296].
[61] E. Komatsu *et al.*, ApJS **192**, 18 (2011), [arXiv:1001.4538].
[62] R. E. Smith *et al.*, MNRAS **341**, 1311 (2003), [arXiv:arXiv:astro-ph/0207664].
[63] E. Semboloni, H. Hoekstra, J. Schaye, M. P. van Daalen and I. G. McCarthy, MNRAS **417**, 2020 (2011), [arXiv:1105.1075].
[64] C. Heymans *et al.*, MNRAS **432**, 2433 (2013), [arXiv:1303.1808].
[65] J. Benjamin *et al.*, MNRAS **431**, 1547 (2013), [arXiv:1212.3327].
[66] Planck Collaboration *et al.*, A&A **571**, A16 (2014), [arXiv:1303.5076].
[67] M. Takada and S. Bridle, New Journal of Physics **9**, 446 (2007), [arXiv:0705.0163].
[68] M. Takada and D. N. Spergel, MNRAS **441**, 2456 (2014), [arXiv:1307.4399].
[69] M. Sato *et al.*, ApJ **701**, 945 (2009), [arXiv:0906.2237].